Parasitic Capacitances, Inductive Coupling, and High-Frequency Behavior of AMR Sensors

Neoclis G. Hadjigeorgiou, *Student Member, IEEE*, and Paul P. Sotiriadis, *Senior Member, IEEE*

***Abstract*—Anisotropic Magneto-Resistive (AMR) sensors are popular in sensitive applications, especially in planar on-chip integrated form which implies the presence of several on-chip capacitive and inductive parasitic elements. However, there is a lack of equivalent circuit models capturing these parasitics and allowing the modeling of sensors' behavior at higher frequencies or in stability-sensitive closed-loop operation. This work fills this gap in the literature by introducing a high-frequency equivalent circuit model, for planar on-chip AMR sensors with integrated offset and Set/Reset coils, capturing the main capacitive and inductive parasitic elements. A general methodology for estimating the values of the parasitic elements via a set of measurements is presented and it is applied to a particular commercial AMR sensor. Using the introduced circuit model, the transfer function from the offset coil voltage to the output voltage of the sensor, via the parasitic capacitive coupling path, is derived. The transfer function from the S/R coil voltage to the offset coil voltage is also derived. Both are used to create a system-level model of the AMR sensor which can be used in system-level analysis to help the designer predict and optimize the open or the closed-loop sensor circuit system behavior. The introduced high-frequency equivalent circuit model and the two related transfer functions have been verified experimentally using the component values derived from the examined commercial AMR sensor.**

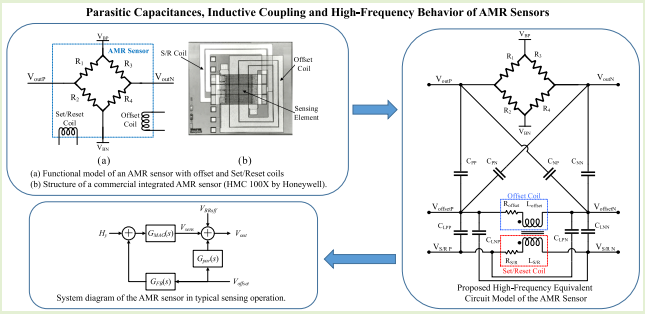

***Index Terms*—Magnetic devices, magnetic sensors, magnetoresistance, anisotropic magnetoresistance, AMR, parameter estimation, model checking.**

I. Introduction

OVER the past decades magnetic sensors have emerged as the preferred choice in many sensor systems due to their high accuracy, reliability and mechanical robustness [1]–[4]. The absence of moving parts enhances their reliability allowing them to operate even under extreme environmental conditions.

Magnetic sensors have a plethora of applications. They are considered a key component of Inertial Measurement Units (IMU) used in navigation systems. Magnetic sensors are also commonly used in the industry for Magnetic Anomaly Detection (MAD), current measurement, detection of rotor position and speed, etc. Consumer applications include, but are not limited to, printers, scanners, cameras, smartphones, computers, electronic compasses, etc. [5], [6]–[13], [14].

There are several types and categories of magnetic sensors on the basis of their sensing principle and manufacturing processes, both of which relate to important parameters, such as manufacturing costs, operating temperatures, frequency response, measurement range and most importantly the obtained resolution and uncertainty [1], [3], [4], [6], [15]–[17]. Some magnetic sensors exhibit a linear response, while others exhibit a non-linear one and hysteresis effects. Also, high accuracy measurements typically come at the cost of slow response. The selection of a sensor depends on the particular application and the main features required, e.g., [1]–[4], [6], [10], and [15]–[19].

Anisotropic Magneto Resistive (AMR) sensors offer an excellent balance between high resolution, high-frequency response, and moderate cost [1]–[3], [16]. Modern integration technologies make their fabrication possible in planar structures, enabling mass production and miniaturization. Unlike magnetic sensors based on the Giant Magnetoresistance, the Giant Magneto-Impedance and the Flux-Gate effects, the AMR based ones feature a more linear behavior in an open-loop configuration [1]–[3], [6], [16], [20].

AMR sensors are typically formed of four anisotropic magnetoresistors in a Wheatstone bridge configuration. Since the magnetoresistance has an even function behavior with respect to the magnetic field, as shown in Fig. 1a, a single magnetoresistor cannot differentiate between positive and negative values of the field [1]–[4], [6], [7], [16]. To overcome this constraint,

Manuscript received September 2, 2019; revised November 7, 2019; accepted November 7, 2019. Date of publication November 13, 2019; date of current version February 5, 2020. The associate editor coordinating the review of this article and approving it for publication was Prof. Tien-Kan Chung. *(Corresponding author: Neoclis G. Hadjigeorgiou.)*

The authors are with the Department of Electrical and Computer Engineering, National Technical University of Athens, 15780 Athens, Greece (e-mail: nhatzig@central.ntua.gr).

Digital Object Identifier 10.1109/JSEN.2019.2953351

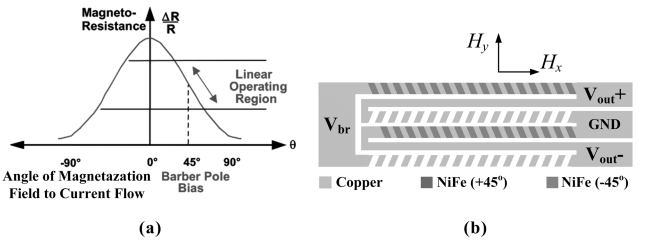

Fig. 1. (a) Magneto-Resistance variation with respect to the angle of the magnetic domains. H_x is the easy magnetic axis and H_y is the sensitivity axis. (b) Anisotropic Magneto-Resistor (AMR) element sensor structure.

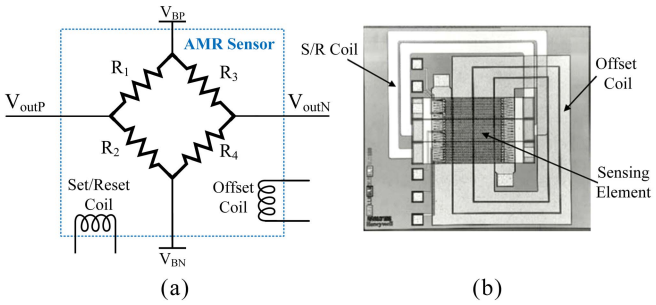

Fig. 2. (a) Functional model of an Anisotropic Magneto-Resistive (AMR) sensor with offset and Set/Reset coils (b) Structure of a commercial integrated AMR sensor (HMC 100X by Honeywell).

the four magnetoresistors of the bridge are split into segments which are positioned in opposite 45° angles as illustrated in Fig. 1b [1]–[5].

The sensing elements are manufactured using a thin-film Ni-Fe permalloy and are deposited on a wafer with typical thickness of 10-100 nm [6], [15], [16]. To achieve a reasonable total Ohmic resistance, in the order of kΩ, several segments are connected in series [1]–[5]. Note that the total resistance should be relatively large, to bias the bridge with a small current, e.g. mA, but at the same time it should be relatively small to result in large bandwidth (small RC product) when the sensor's output is connected to a voltage amplifier. The total size of the bridge is in the order of 1mm, i.e. relative larger than Hall sensors and significantly smaller than traditional Flux-Gate ones.

Despite the advantages mentioned above, AMR sensors still suffer from certain deficiencies, such as: DC offset, magnetic hysteresis, cross-axis effects, required periodic re-polarization of the permalloy film magnetic domains and degradation of linear response when operating outside of a certain range of the magnetic field [2], [15], [16], [21]–[23]. Therefore there is room for considerable improvement [4], [16], [23]–[29].

Some of the aforementioned issues can be partially addressed by introducing a Set/Reset coil (strap) and an offset coil (strap) [1]–[4], [6], [9], [15], [16], [21], [30]. The offset coil can be used for closed-loop feedback and offset cancelling [1]–[4], [6], [9], [15], [16], [21], [30], while the Set/Reset (S/R) coil (strap) can be used for the re-polarization of the magnetic domain. Such a configuration is illustrated in Fig. 2a where the two coils and the sensing element of the AMR sensor are shown. The coils are supposed to be mutually inductively decoupled, with the offset coil be coupled to the hard-magnetic axis (sensitive axis) and the S/R coil be coupled to the easy-magnetic axis. Re-polarization is the main technique used to reduce the sensor's gain degradation, due to demagnetization, and potentially minimize sensor's offset [1]–[4], [6], [15], [16], [21], [23].

AMR sensors are widely used and several behavioral models of them exist in the literature [1]–[32]. However, to the best of our knowledge, all of the proposed models account only for the DC behavior of the sensors, even though, there are applications where AMR sensors are used in MHz - range frequencies, e.g. [31], [32]. Furthermore, in closed-loop architectures (using the feedback coil) one must account for the loop phase and amplitude at frequencies much higher than the closed-loop bandwidth of the sensor, to ensure stability. Thus, in such cases, a broadband (DC to high frequency) behavioral model of the sensor is mandatory.

In this work, the broadband behavior of the popular commercial AMR sensor HMC100X is investigated in detail. The HMC100X sensor is integrated, has an open-loop bandwidth of 5 MHz [21] and a planar structure shown in Fig. 2. It includes an offset and a Set/Reset coil which are packed tightly with the AMR sensing elements. These result in the presence of on-chip capacitive and inductive parasitic couplings which directly impact the high(er) frequency behavior of the complete sensor (chip) even at sub-MHz frequencies, as it is shown in Section III-B. The knowledge of the sensor's parasitics helps in the optimization of open-loop architectures and enables the design of high-performance closed-loop architectures, operating in higher frequencies.

The contributions of this work are the followings: 1) A high-frequency equivalent circuit model of the AMR sensor is introduced, 2) A methodology for the experimental estimation of the parasitic capacitances and the self and mutual inductances of the model is presented. The effects of these parasitic elements on the sensor's performance are examined. 3) The model is benchmarked in a series of experiments.

The remainder of this paper is organized as follows. In Section II, the proposed high-frequency equivalent circuit model of the AMR sensor is introduced. In Section III the parasitic capacitances of the model are estimated and verified. Additionally, the transfer function of the AMR sensor with its' parasitic capacitances is introduced. Section IV presents the derivation of the self and mutual inductances of the model. Section V introduces a simplified but complete system-level diagram of the AMR sensor based on the transfer function derived in Section III. Finally, Section VI summarizes this research findings and concludes the paper.

II. High-Frequency Sensor Model

The high-frequency model introduced here focuses on the parasitic capacitances and inductances of the sensor, namely: i) the capacitances between the offset coil and the bridge, ii) the capacitances between the offset and the S/R coils, and, iii) the magnetic coupling between the offset and the S/R coils.

The parasitic capacitances between the S/R coil and the bridge are negligible and can be ignored. This is because the bridge is placed at the top, the S/R coil is placed at the bottom and the offset coil is between them providing an electric field isolation, as shown in Fig. 2.

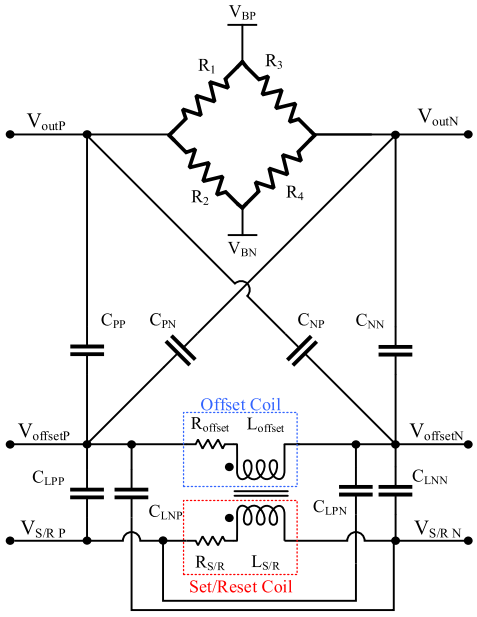

Fig. 3. Proposed high-frequency equivalent circuit model of the AMR sensor.

The above covers all pair-wise parasitic elements between the bridge and the offset and S/R coils. The parasitic capacitances between them and the substrate or the package are considered less important.

Furthermore, it is assumed that the sensor in Fig. 2 operates in the linear region. This is typically the case when the sensor operates in a closed-loop configuration where the current of the offset coil is the feedback signal that ideally zeros the total magnetic field on the sensing elements.

Also, it is assumed that the sensor's magnetic state has been set to maximum sensitivity before the measurements. To this end, a sequence of positive (Set) current pulses have passed through the S/R coil.

The proposed high-frequency circuit model of the AMR sensor is shown in Fig. 3, where:

i) $C_{PP}, C_{PN}, C_{NP}, C_{NN}$: are the lumped approximations of the distributed parasitic capacitances between the offset coil and the sensing elements.

ii) $C_{LPP}, C_{LPN}, C_{LNP}, C_{LNN}$: are the lumped approximations of the distributed parasitic capacitances between the offset and the S/R coils.

iii) The magnetic coupling between the offset and the S/R coils is captured by the transformer symbol, with core, due to the sensor's ferromagnetic material.

The sensing elements R_1, R_2, R_3, R_4 form a Wheatstone bridge. Resistors R_1 and R_4 vary with the magnetic field strength simultaneously and oppositely to R_2 and R_3.

In general the electrical resistance of a sensing element can be modeled as $R_0 + \Delta R \cdot \cos^2(\theta)$, where R_0 is insensitive to the magnetic field and θ is the rotation angle of the magnetic dipoles [1]–[3], [24]. In a weak magnetic field, the resistance of a sensing element with barber pole structure is approximately

$$R\left(H_y\right) = R_0 + \Delta R \cdot \left[1 - \left(\frac{H_y - M_y}{H_0}\right)^2\right]. \quad (1)$$

Where ΔR is the sensitivity factor, H_0 is the characteristic magnetic field of the sensing element, M_y is the magnetization of the sensing element when it is placed in a barber pole structure and H_y is the magnetic field projected on the y axis of the element (perpendicular to the current bias), see Fig. 1. Equation (1) can be further simplified as

$$R\left(H_y\right) = R_0 + r \cdot H_y \quad (2)$$

where r is the first-order coefficient of the Taylor series expansion of (1).

III. Derivation of the Parasitic Capacitances

The values of the parasitic capacitances C_{PP}, C_{PN}, C_{NP} and C_{NN}, between the sensing elements and the offset coil, are derived using four different circuit configurations of the sensor. They are also verified via an additional set of measurements.

In both cases the sensor is set to high sensitivity by passing a sequence of Set (positive) current pulses through the S/R coil, just before the measurements.

A. Capacitor Estimation

Assuming the high-frequency equivalent circuit model of the AMR sensor in Fig. 3, the capacitances C_{PP}, C_{PN}, C_{NP} and C_{NN} are estimated using the four different configurations of the model shown in Fig. 4. Here, the sensing element's terminals, V_{BP} and V_{BN} are grounded and $R_{thP} = R_1//R_2$, $R_{thN} = R_3//R_4$ represent the equivalent Thévenin resistances of the terminals, respectively.

In all cases, one side of the offset coil ($V_{offsetP}$ or $V_{offsetN}$) is grounded while the other one is driven by the sinusoidal signal V_{AC} of fixed amplitude and frequency ranging from 10kHz to 1MHz. Since the voltages at the nodes $V_{offsetP}$ and $V_{offsetN}$ are set, the parasitic capacitances C_{LPP}, C_{LPN}, C_{LPN} and C_{LNN}, as well as the offset coil and its magnetic coupling to the S/R coil (Fig. 3) do not impact significantly the currents and voltages of the sensing elements R_1 to R_4 and are ignored in the schematic of Fig. 4. Finally, the amplitude of the sinusoidal voltage at V_{outP} or V_{outN} is measured using an oscilloscope in configurations a, b, c and d, in Fig. 4 respectively. The parasitic resistor R_P and capacitor C_P of the probe as well as the input impedance of the oscilloscope are taken into account.

Capacitances C_{PP}, C_{PN}, C_{NP} and C_{NN}, are derived using only the magnitude of the transfer function $V_{outP}(s)/V_{AC}(s)$ measured at a number of frequency points ω_k, $k = 1, 2, \ldots, N$. Consider the configuration in Fig. 4a for example which gives

$$V_{outP}(s) = \frac{sC_{PP}R_{thP}}{s\left(C_{PP} + C_{PN} + C_P\right)\left(R_{thP}//R_P\right) + 1} V_{AC}(s) \quad (3)$$

from which we get that

$$\left|\frac{V_{AC}(\omega_k)}{V_{outP}(\omega_k)}\right|^2 = A \cdot x_k + B \quad (4)$$

where we have set $x_k = 1/\omega_k^2$, $A = 1/\left(C_{PP}R_{thP}\right)^2$ and $B = \left(C_{PP} + C_{PN} + C_P\right)^2 \left(R_{thP}//R_P\right)^2 / \left(C_{PP}R_{thP}\right)^2$. Since (4) is linear in x_k we use least squares linear regression to estimate

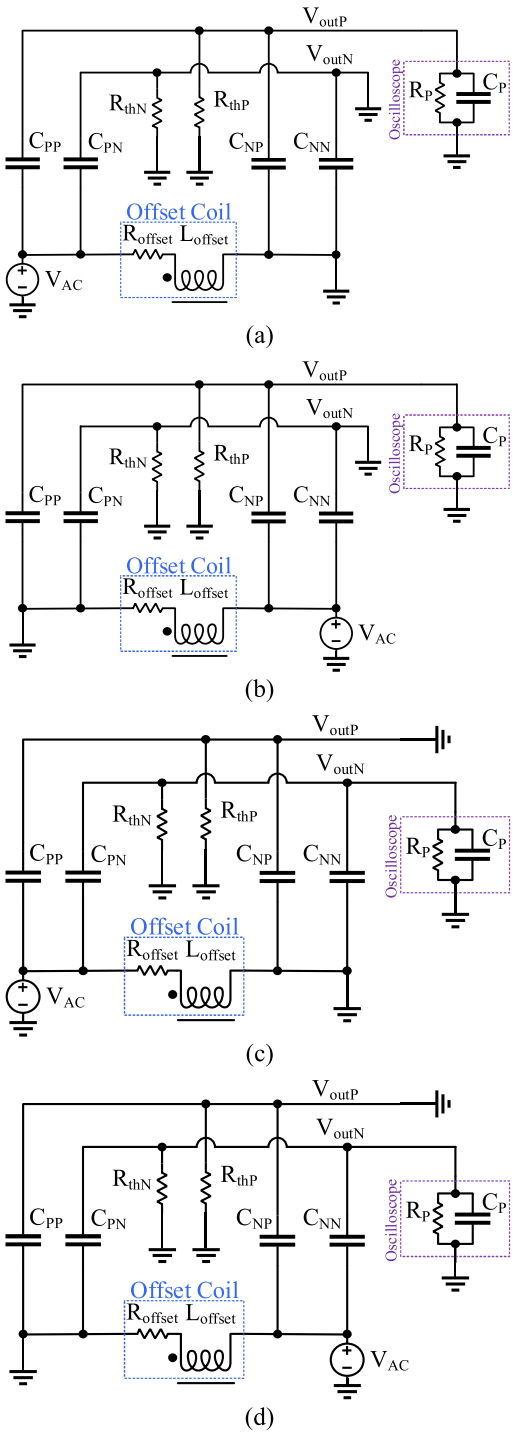

Fig. 4. Measuring configurations for capacitance estimation: (a) for C_{PP}, (b) for C_{NP}, (c) for C_{PN}, and (d) for C_{NN}.

A and B. Since R_{thP} is easy to measure directly (see Table I) the value of C_{PP} is derived using A and R_{thP}. Finally, note that the unknown value of C_{PN} does not pose a problem in the estimation, since C_{PP} appears solely on the nominator of the transfer function.

The rest of the capacitances C_{PN}, C_{NP} and C_{NN} are derived similarly based on the corresponding configuration (Fig. 4b-4d) and the general relationship:

$$V_{out}(s) = \frac{sC_X R_{thX}}{s\left(C_X + C_Y + C_P\right)\left(R_{thP} // R_P\right) + 1} V_{AC}(s) \quad (5)$$

TABLE I
MEASURED VALUE OF THE RESISTOR (DC & ZERO BIAS)

Resistor	Set Value	Reset Value
R_1	825Ω	823Ω
R_2	824Ω	824Ω
R_3	828Ω	825Ω
R_4	828Ω	826Ω

TABLE II
ESTIMATED VALUE OF THE PARASITIC CAPACITANCE

Capacitor	Value
C_{PP}	27.5pF
C_{PN}	9.8pF
C_{NP}	10.3pF
C_{NN}	25.7pF

where C_X is the capacitor of interest, C_Y is the other parasitic capacitance, C_P is the probe capacitance and R_{thX} is the Thévenin equivalent resistance of the bridge parallel to the probe's resistance R_P.

The resistances of the sensing elements R_1, R_2, R_3 and R_4, measured with zero bias, are shown in Table I. The estimated values of the capacitances C_{PP}, C_{PN}, C_{NP} and C_{NN} are presented in Table II.

The measurements were conducted using a function generator to provide V_{AC}, a low-noise voltage preamplifier with impedance at the probe $R_P = 100\text{M}\Omega$ in parallel with $C_P = 25pF$, and, a digital oscilloscope to measure the amplitude at the output of the preamplifier. Ambient temperature was maintained around 21°C±1°C.

It is worth mentioning that the Ohmic resistances of the sensing elements (R_1, R_2, R_3 and R_4) depend on the applied magnetic field. Therefore, the generated magnetic field, during the measurements, due to the current through the offset coil should remain small, e.g. less than 2mA. This constrains accordingly the amplitude of V_{AC}.

Finally, the sum of the capacitors C_{LPP}, C_{LPN}, C_{LPN} and C_{LNN} is measured directly using an RLC meter with a Kelvin sensing probe. The capacitors represent a lumped equivalent model of the distributed capacitances between the offset and the S/R coils. The geometrical structure of the integrated AMR sensor in Fig. 2b indicates that is should be approximately $C_{LPP} \approx C_{LPN} \approx C_{LNP} \approx C_{LNN}$.

B. Capacitor Model Verification

To check the accuracy of the derived capacitor values, another test was performed based on a differential setup of the proposed equivalent circuit model in Fig. 3. The setup is shown in Fig. 5 in two variations, with and without bias of the bridge.

In both cases (Fig. 5a and 5b) a sinusoidal signal source, V_{AC}, of fixed amplitude and frequency ranging from 10kHz to 1MHz, is connected between $V_{offsetP}$ and $V_{offsetN}$, and, the resulting voltage difference between V_{outP} and V_{outN} is measured. Going from the model in Fig. 3 to the test cases in Fig. 5a and 5b, the parasitic capacitances C_{LPP}, C_{LPN}, C_{LPN} and C_{LNN} as well as the S/R coil are ignored since they do not impact the measurement significantly.

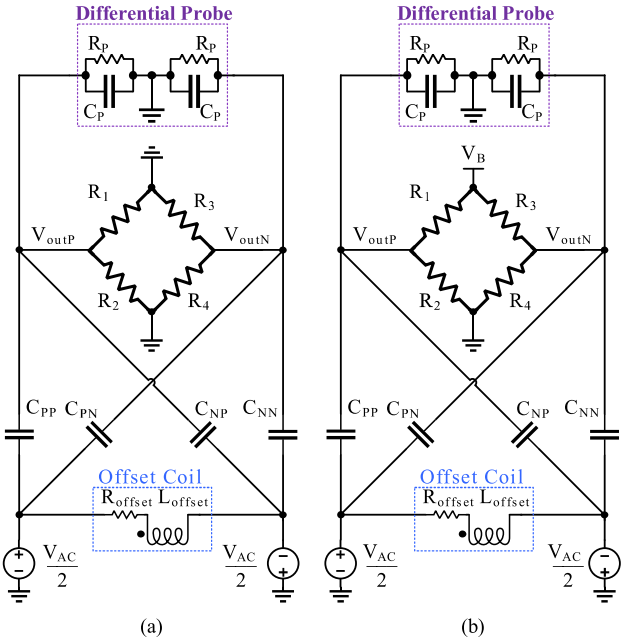

Fig. 5. Equivalent circuit for model verification (a) without and (b) with voltage bias.

1) Case 1: Without Bridge Bias: Following the schematic in Fig. 5a, the bridge is unbiased and therefore the Ohmic resistances R_1, R_2, R_3 and R_4 of the sensing elements are as in the schematics in Figs. 4a-d, given in Tables I and II. Accurately predicting the output voltage $V_{outP} - V_{outN}$ with the derived capacitor values is the first step for validating our model and component value derivation process.

Since the bridge is not biased, the ambient magnetic field as well as that generated by the current of the offset coil do not impact the voltage difference $V_{outP} - V_{outN}$ in the first order. This is because $R_{thP} = R_1//R_2$ and $R_{thN} = R_3//R_4$ ideally are not sensitive to the magnetic field in the first Taylor order. Recall that R_1 and R_4 increase or decrease with the magnetic field simultaneously and oppositely to R_2 and R_3, and all of them have the same nominal value. Diversions from this assumption as well as strong magnetic field (which appears as a 2nd order Taylor term in R_{thP} and R_{thN}) can introduce a small signal modulation due to time-dependent R_{thP} and R_{thN}, and therefore higher order harmonics at the output. To avoid this, V_{AC} is small to ensure that R_{thP}, R_{thN} vary by less than 1%.

The transfer function of the circuit in Fig. 5a defined as $\mathrm{G}_{par}(\mathrm{s}) \triangleq (\mathrm{V_{outP}}(s) - \mathrm{V_{outN}}(s))/\mathrm{V}_{AC}(s)$ is given by

$$\mathrm{G}_{par}(\mathrm{s}) = \frac{1}{2}\left[\frac{R_{thP}(C_{PP}-C_{NP})s}{R_{thP}(C_{PP}+C_{NP})s+1} + \frac{R_{thN}(C_{NN}-C_{PN})s}{R_{thN}(C_{NN}+C_{PN})s+1}\right] \quad (6)$$

Note that the probe's resistance R_P is $100M\Omega$ and it is ignored in (6). Also, the probe's capacitance C_P is $25pF$, which at $1MHz$ has an imaginary impedance of about $6.4k\Omega$. This is about 15 times larger than R_{thP} and R_{thN}, and, since the frequency range is up to $1MHz$ capacitance C_P can be safely ignored as well.

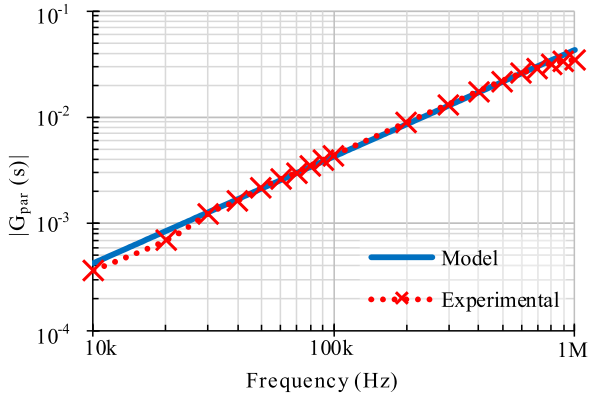

Fig. 6. Comparison of the model and the experimental $|\mathrm{G}_{par}(\mathrm{s})|$ versus frequency, without voltage bias of the sensor bridge.

Transfer function $\mathrm{G}_{par}(\mathrm{s})$ is derived numerically based on equation (6), and, experimentally based on the setup in Fig. 5a. Both results appear in Fig. 6.

The experiment was performed at an ambient temperature of 22°C±1°C. The graph in Fig. 6 suggests that the model is in satisfactory agreement with experimental data. The linear error between the measured data and the model-based calculations is less than 6% in the range of 30kHz to 1MHz. At frequencies below 30kHz, the error is higher due to the measuring equipment limitations. Note that $G_{par}(s)$ is a high pass filter resulting in very low output amplitude at low frequencies.

2) Case 2: With Bridge Bias: Following the schematic in Fig. 5b the bridge is biased as typically done in open and closed-loop architectures. The total transfer function is defined as

$$\mathrm{G}(\mathrm{s}) \triangleq (\mathrm{V_{outP}}(s) - \mathrm{V_{outN}}(s))/\mathrm{V}_{AC}(s)$$

and it is expressed as the sum of two transfer functions, i.e.

$$G(s) = G_{par}(s) + \delta \cdot G_{sens}(s), \quad \text{with } \delta = \pm 1 \quad (7)$$

The first term, $\mathrm{G}_{par}(\mathrm{s})$, given by equation (6), captures the contribution of the input differential voltage V_{AC} to the voltage difference between V_{outP} and V_{outN} via the direct parasitic signal path of C_{PP}, C_{PN}, C_{NP} and C_{NN}. The second one, $\mathrm{G}_{sens}(\mathrm{s})$ captures the sensing elements' resistance variation due to the magnetic field generated by the current passing through the offset coil when it is excited by V_{AC}. Finally, multiplier $\delta = \pm 1$ depends on whether the sensor is in the Set (+1) or the Reset (−1) state.

To derive $\mathrm{G}_{sens}(\mathrm{s})$ in (7) we start from (2) and express the resistances of the sensing elements as $R_{1,4} = R_0 - r \cdot H_y$ and $R_{2,3} = R_0 + r \cdot H_y$ respectively. Recall that the two pairs are influenced in opposite way by the magnetic field and their variations are small due to assumed small V_{AC} amplitude, justifying a linear approximation.

Furthermore, the magnetic field can be expressed as $H_y = \alpha \cdot I$, for some conversion factor α (in Tesla / Ampere), where $I = V_{AC}/\left(R_{offset} + s \cdot L_{offset}\right)$ is the current through the offset coil due to V_{AC}.

Making the approximation $C_{PP} + C_{NP} \approx C_{NN} + C_{PN}$ based on the values in Table II ($37.8pF$ Vs. $35.5pF$), and,

setting $C_T = C_{PP} + C_{NN} + C_{NP} + C_{PN}$, the transfer function $G_{sens}(s)$ is expressed as

$$G_{sens}(s) = \frac{4\alpha \cdot r \cdot V_B}{R_0 (s \cdot R_0 C_T + 4)\left(R_{offset} + s \cdot L_{offset}\right)} \quad (8)$$

Note that the probe impedances $(R_P // C_P)$ in Fig. 5b are ignored as they are not part of the sensor's model.

As expected, G_{par} (s) in (6) is a high-pass transfer function with $G_{par}(0) = 0$. Also $G_{sens}(s)$ is a 2nd order low-pass transfer function with $G_{sens}(0) = \alpha \cdot r \cdot V_B / \left(R_0 \cdot R_{offset}\right)$.

To evaluate the impact of the parasitic path $G_{par}(s)$, it is convenient to examine the total transfer function normalized at zero frequency for the Set and Reset states of the bridge, i.e.,

$$\hat{G}_{SET}(s) \left.\frac{G(s)}{G(0)}\right|_{\delta=+1} = \frac{G_{par}(s)}{G_{sens}(0)} + \frac{G_{sens}(s)}{G_{sens}(0)}$$
$$\hat{G}_{RESET}(s) \left.\frac{G(s)}{G(0)}\right|_{\delta=-1} = \frac{G_{par}(s)}{G_{sens}(0)} - \frac{G_{sens}(s)}{G_{sens}(0)}. \quad (9)$$

The transfer functions $\hat{G}_{SET}(s)$ and $\hat{G}_{RESET}(s)$ are calculated analytically via (9) using the derived component values in Tables I and II. They are also measured experimentally using the setup in Fig. 5b.

Note that the impedances to ground of the low-frequency probe, used up to 1 MHz, where 25 pF//100 MΩ. Also, the differential impedance of the high-frequency probe, used between 1 MHz and 10 MHz, was 4 pF//15 kΩ. In both cases, the impedances are significantly larger than R_{thP} and R_{thN}, and can be ignored for the purposes of this work.

The amplitude and phase of both $\hat{G}_{SET}(s)$ and $\hat{G}_{RESET}(s)$ appear in Fig. 7. In the experimental setup we used $V_B = 5V$ for biasing the bridge and the ambient temperature was 22°C±1°C. To get the experimental value of $G(0)$ the offset voltage of the setup was measured and subtracted.

Note that in low frequencies $\hat{G}_{SET}(s)$ and $\hat{G}_{RESET}(s)$ in (9) are close to one and so $G_{sens}(s)$ is the dominant part of $G(s)$ in (7). In higher frequencies, the effects of parasitic capacitors dominate $G(s)$.

In both Set and Reset states, the percentile amplitude error of $\hat{G}_{SET}(s)$ and $\hat{G}_{RESET}(s)$, between the model and the measurements is less than 6% and the percentile phase error is less than 7%, over the whole measured frequency range.

Note that since the sensor bridge is biased, it is highly sensitive to the magnetic field generated by external sources (e.g. EMI from measuring equipment, fluorescent lights etc.). Therefore, the measurement is sensitive and very susceptible to errors due to external interference. Ideally, it has to be done within a magnetic field shield (Gauss chamber). Moreover, the amplitude of V_{AC} must be small to avoid exciting nonlinear behavior and introduction of higher order harmonics.

The relatively small error in the amplitude and the phase indicates that the proposed high-frequency equivalent circuit model of the AMR sensor in Fig. 3 and the estimated component values are satisfactory for most applications.

IV. Derivation of Self and Mutual Inductance

The offset and the S/R coils, which are coupled with the hard-magnetic axis and the easy-magnetic axis of the sensing elements, respectively, should be inductively decoupled; ideally, they should be geometrically orthogonal.

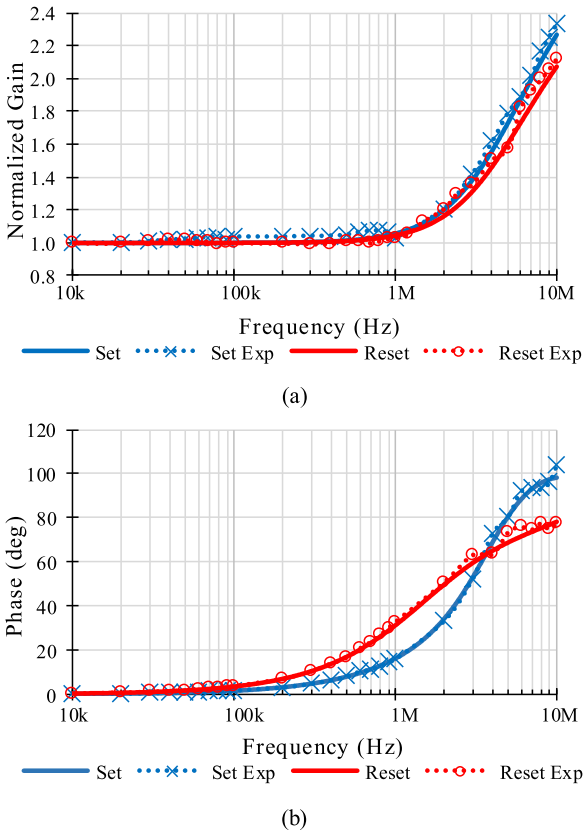

Fig. 7. Model-based and experimental (a) Normalized Gain and (b) Phase of $\hat{G}_{SET}(s)$ and $\hat{G}_{RESET}(s)$, with voltage biased sensor bridge. Blue lines correspond to the Set state and red lines correspond to the Reset state.

In the planar chip configuration however, the situation is far from ideal as shown in Fig. 2. The parasitic inductive coupling between the two coils is captured in the proposed high-frequency model in Fig. 3 with the transformer symbol.

In typical open or closed loop operation of the sensor, the magnetic field measurement interval follows a Set or Reset interval. During the measurement interval, the S/R coil can be open-circuited to avoid any inductive current that would affect the magnetization of the sensing element (in the easy axis). During the S/R interval however, the current through the S/R coil can result in an unwanted voltage at the offset coil due to parasitic magnetic coupling between the two coils.

Even if the measurement and the S/R intervals do not overlap, the parasitic voltage at the offset coil can be disturbing in some sensor's architectures. It is therefore useful to estimate not only the values of the components in the proposed model, but also the impact of the voltage of the S/R coil on the voltage of the offset coil.

A. Self and Mutual Inductance Estimation

Consider the proposed high-frequency model in Fig. 3. The self-inductance and the equivalent series resistance of the offset and the S/R coils are measured directly using an LCR meter. To minimize the measurement error due to the

TABLE III
MEASURED VALUE OF THE PARASITIC CAPACITANCE

Capacitor	Value
$C_{LPP} \approx C_{LPN} \approx C_{LNP} \approx C_{LNN}$	13.75pF

TABLE IV
MEASURED VALUE OF COIL COUPLING PARAMETERS

Parameter	Value
L_{offset}	75nH
R_{offset}	2.6Ω
$L_{S/R}$	56nH
$R_{S/R}$	1.5Ω
M	13nH
k	0.2

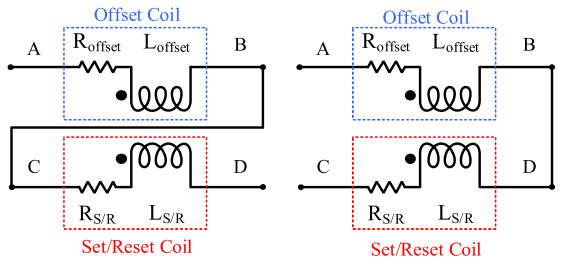

Fig. 8. Estimation of the mutual inductance in a lossy transformer by measuring impedances Z_{AD} and Z_{AC}.

parasitic capacitors C_{PP}, C_{PN}, C_{NP}, C_{NN}, C_{LPP}, C_{LPN}, C_{LPN} and C_{LNN}, the excitation frequency of the LCR meter was 1 kHz. At 1 kHz, the capacitors impedance magnitude is larger than 5 MΩ (Section III-A, Table II & Table III), and therefore they can be safely ignored. The measured values of L_{offset}, R_{offset}, $L_{S/R}$ and $R_{S/R}$ are given in Table IV.

One way to derive the mutual inductance M and the coupling coefficient k in a lossy transformer is by measuring impedances Z_{AB} and Z_{AC} as illustrated in Fig. 8. Since

$$\begin{aligned} Z_{AD}(s) &= \left(L_{offset} + L_{S/R} + 2M\right) \cdot s + R_{offset} + R_{S/R} \\ Z_{AC}(s) &= \left(L_{offset} + L_{S/R} - 2M\right) \cdot s + R_{offset} + R_{S/R} \end{aligned} \tag{10}$$

the mutual inductance is given by $M = (L_{AD} - L_{AC})/4$, where $L_{AD} = L_{offset} + L_{S/R} + 2M$ and $L_{AC} = L_{offset} + L_{S/R} - 2M$ are measured with the LCR meter. Again the excitation frequency of the LCR meter was set to 1 kHz to avoid any impact of the parasitic capacitances C_{PP}, C_{PN}, C_{NP}, C_{NN}, C_{LPP}, C_{LPN}, C_{LPN} and C_{LNN}. Finally, the coupling coefficient is derived using $k = M/\sqrt{L_{offset} \cdot L_{S/R}}$.

The measurements give $L_{AD} = 234$nH and $L_{AC} = 207$nH. All component values of transformer are given in Table IV. All measurements were conducted at ambient temperature of 21°C±1°C.

B. S/R to Offset Coil Voltage Transfer Function

A way to capture the impact of the S/R pulses on the offset coil is by deriving the voltage transfer function from the first to the second one, i.e. $G_C(s) \triangleq (V_{offsetP}(s) - V_{offsetN}(s))/V_{AC}(s)$ as shown in Fig. 9. Note that in the frequency range we consider, the resistance of the bridge is very small compared to the impedance of the capacitors C_{PP}, C_{PN}, C_{NP} and C_{NN}. Therefore, the capacitors can be assumed to be grounded at the bridge's side.

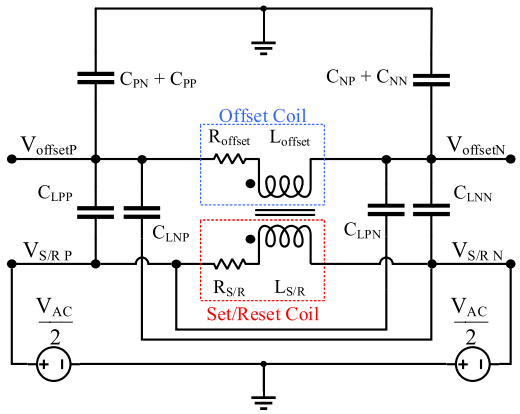

Fig. 9. Capturing the impact of the S/R coil voltage to the offset coil voltage.

With this assumption we have that

$$G_C(s) = \frac{1}{2} \cdot \frac{A_3 \cdot s^3 + A_2 \cdot s^2 + A_1 \cdot s + A_0}{B_3 \cdot s^3 + B_2 \cdot s^2 + B_1 \cdot s + B_0} \tag{11}$$

where

$$\begin{aligned} A_3 &= X\,(C_A + 2C_{LA}) \\ A_2 &= Y\,(C_A + 2C_{LA}) \\ A_1 &= (C_A + 2C_{LA})\,R_{offset} \cdot R_{S/R} + 2M \cdot C_{TT} \\ A_0 &= 0 \\ B_3 &= C_D \cdot X \\ B_2 &= C_D \cdot Y \\ B_1 &= C_D \cdot R_{offset} \cdot R_{S/R} + C_{TT} \cdot L_{S/R} \\ B_0 &= R_{S/R} \cdot C_{TT} \end{aligned}$$

and

$$\begin{aligned} C_{TT} &= C_{BP} + C_{BN} + C_{LPP} + C_{LPN} + C_{LNP} + C_{LNN} \\ C_A &= (C_{LPP} - C_{LNP})\,C_{BN} + (C_{LNN} - C_{LPN})\,C_{BP} \\ C_{BP} &= C_{PN} + C_{PP} \\ C_{BN} &= C_{NP} + C_{NN} \\ C_D &= (C_{LPP} + C_{LNP} + C_{BN})\,(C_{LNN} + C_{LPN} + C_{BP}) \\ C_{LA} &= C_{LPP} \cdot C_{LNN} - C_{LNP} \cdot C_{LPN} \end{aligned}$$

as well as

$$\begin{aligned} X &= L_{S/R} \cdot L_{offset} - M^2 \\ Y &= L_{S/R} \cdot R_{offset} + R_{S/R} \cdot L_{offset}. \end{aligned}$$

C. Self and Mutual Inductance Model Verification

To verify the accuracy of the derived self and mutual inductance values, the transfer function $G_C(s)$ was estimated via (11) and was compared to measured values. To this end,

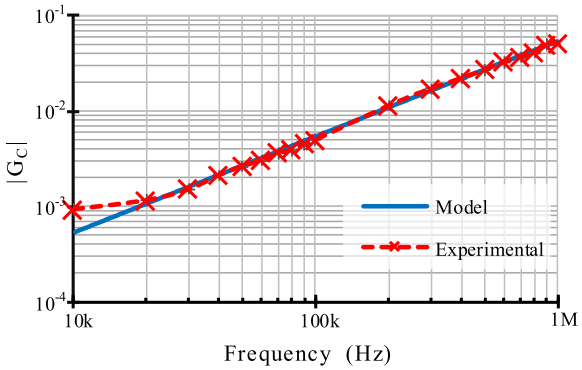

Fig. 10. Comparison between the model-based calculation and the experimental measurement of $|G_C(s)|$, following the schematic in Fig. 9.

a sinusoidal V_{AC} of fixed amplitude, and frequency ranging from 10 kHz to 1 MHz, was applied differentially between V_{S/R_P} and V_{S/R_N}, and, the voltage between $V_{offsetP}$ and $V_{offsetN}$ was measured as shown in Fig. 9.

The results are shown in Fig.10 indicating an error of $|G_C(s)|$, of about 7% from 20 kHz to 1 MHz. Below 20 kHz there is a significant error due to the limited sensitivity of the instruments. All measurements were performed at ambient temperature 21°C±1°C.

The results suggest that feedthrough is present from the Set/Reset coil to the offset coil and becomes significant with frequency increasing. Therefore, S/R pulsing may induce current to the offset coil, especially when the last one is connected to a low output-impedance driver. This may have significant impact on the measurement quality in closed-loop architectures if the loop operates continuously.

V. System Diagram of the AMR Sensor

A system block diagram of the AMR sensor, in typical sensing operation, based on the high-frequency model of Fig. 3, is shown in Fig. 11.

Suppose that the sensor is exposed to an external magnetic field H_y and a voltage $V_{offset} \triangleq V_{offsetP} - V_{offsetN}$ is applied to the offset coil. Then, the output voltage, $V_{out} \triangleq V_{outP} - V_{outN}$, of the sensor (without load) is the sum of three terms:

1) The internal DC offset voltage of the bridge, i.e.,

$$V_{BRoff} = \left(\frac{R_2}{R_1+R_2} - \frac{R_4}{R_3+R_4}\right)\Bigg|_{H_y=0} \cdot V_B.$$

2) The voltage contribution of V_{offset} to the output due to the parasitic capacitive coupling between V_{offset} and V_{out}, captured by $G_{par}(s)$ in (6).

3) The response of the bridge to the total magnetic field which is the sum of H_y and that generated by the offset coil due to V_{offset}. The contribution of the (possibly time-variant) external magnetic field H_y equals $G_{MAG}(s) H_y(s)$ where, from Section III.B.2 and (2), it is

$$G_{MAG}(s) = \frac{4r \cdot \delta \cdot V_B}{R_0 (s \cdot R_0 C_T + 4)}.$$

Also, the direct contribution of V_{offset} to the output voltage, through the internal magnetic field generation by the offset coil, is $\delta \cdot G_{sens}(s) \cdot V_{offset}(s)$, where $G_{sens}(s)$ is given in (8). It is convenient to write $\delta \cdot G_{sens}(s) \cdot V_{offset}(s) = G_{FB}(s) \cdot G_{MAG}(s)$ where $G_{FB}(s) \triangleq \frac{\alpha}{R_{offset}+s \cdot L_{offset}}$ and α is the current-to-magnetic field conversion factor defined in Section III.B.2

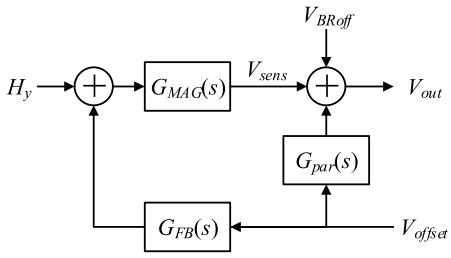

Fig. 11. System diagram of the AMR sensor in typical sensing operation.

In the above analysis it has been assumed that V_{offset} is set by a differential voltage source, as before, and that the S/R coil is floating during the sensing operation. Note that the current injected to the floating S/R coil by V_{offset}, via parasitic capacitors C_{LPP}, C_{LPN}, C_{LPN} and C_{LNN}, is negligible with respect to the current of the offset coil for frequencies up to 1 MHz (since the impedance of C_{LP} and C_{LN} is orders of magnitude higher than that of L_{offset} and R_{offset}).

VI. Conclusion

In this work we introduced a high-frequency equivalent circuit model for the planar on-chip AMR sensor HMC100X capturing the main capacitive and inductive parasitic elements. Using the model, the transfer function from the offset coil voltage to the output of the sensor, via the parasitic capacitive coupling path, has been derived and verified experimentally. The model was also used to derive the transfer function from the S/R coil voltage to the offset coil voltage, capturing the parasitic signals introduced indirectly to the measurements by the S/R pulses, which has also been verified experimentally. Finally, a system diagram of the AMR sensor was introduced which can be used in high level system analysis.

The introduced model can be used as a design and analysis tool in both open- and closed-loop architectures. It can help deriving the sensor system's transfer function and verifying stable operation in the closed-loop cases. Finally, it can be used as a guideline in deriving high-frequency equivalent models for other AMR sensors with offset and S/R coils.

Acknowledgment

The authors would like to thank Prof. J. Georgiou, Director of Holistic Electronics Research Laboratory of the Department of Electrical and Computer Engineering at the University of Cyprus and Prof. E. Hristoforou, Director of Sensors Laboratory of the Department of Electrical and Computer Engineering at the National Technical University of Athens for proving access to their laboratory instruments.

REFERENCES

[1] J. Fraden, *Handbook of Modern Sensors: Physics, Designs, and Applications*, 4th ed. New York, NY, USA: Springer-Verlag, 2010.

[2] P. Ripka, *Magnetic Sensors and Magnetometers*. Norwood, MA, USA: Artech House, 2001.

[3] P. Ripka and A. Tipek, *Modern Sensors Handbook*. Arlington, VA, USA: ISTE, 2007.

[4] S. Tumanski, *Handbook of Magnetic Measurements*, 1st ed. Florida, FL, USA: CRC Press, 2011.

[5] A. Platif, J. Kubik, M. Vopalensky, and P. Ripka, "Precise AMR magnetometer for compass," in *Proc. IEEE Sensors*, Oct. 2003, pp. 472–476.

[6] P. Ripka and K. Závěta, "Magnetic sensors: Principles and applications," in *Handbook of Magnetic Materials*, vol. 18, K. H. J. Buschow, Ed., 1st ed. Amsterdam, The Netherlands: Elsevier, 2009, pp. 347–420.

[7] N. Hadjigergiou, M. Sophocleous, E. Hristoforou, and P. P. Sotiriadis, "Magnetic sensors for space applications: Development and magnetic cleanliness considerations," in *Electromagnetic Compatibility for Space Systems Design*, C. D. Nikolopoulos, Ed., 1st ed. Hershey, PA, USA: IGI-Global, 2018, pp. 248–283.

[8] M. Janosek, J. Vyhnanek, and P. Ripka, "CW metal detector based on AMR sensor array," in *Proc. IEEE Sensors*, Oct. 2011, pp. 1515–1517.

[9] S. Sordo-Ibáñez *et al.*, "A front-end ASIC for a 3-D magnetometer for space applications by using anisotropic magnetoresistors," *IEEE Trans. Magn.*, vol. 51, no. 1, Jan. 2015, Art. no. 4001804.

[10] W. J. Fleming, "Overview of automotive sensors," *IEEE Sensors J.*, vol. 1, no. 4, pp. 296–308, Dec. 2001.

[11] S. Leitner *et al.*, "Design of the magnetoresistive magnetometer for ESA's SOSMAG project," *IEEE Trans. Magn.*, vol. 51, no. 1, Jan. 2015, Art. no. 4001404.

[12] E. Zimmermann, A. Verweerd, W. Glaas, A. Tillmann, and A. Kemna, "An AMR sensor-based measurement system for magnetoelectrical resistivity tomography," *IEEE Sensors J.*, vol. 5, no. 2, pp. 233–240, Apr. 2005.

[13] J. Široké, "Solar storm detecting by integrated magnetometer based on anisotropic magnetoresistivity," in *Proc. 25th Telecommun. Forum (TELFOR)*, Nov. 2017, pp. 1–4.

[14] H. Zhu and F. Yu, "A cross-correlation technique for vehicle detections in wireless magnetic sensor network," *IEEE Sensors J.*, vol. 16, no. 11, pp. 4484–4494, Jun. 2016.

[15] D. J. Mapps, "Magnetoresistive sensors," *Sens. Actuators A, Phys.*, vol. 59, nos. 1–3, pp. 9–19, Apr. 1997.

[16] A. Grosz, M. J. Haji-Sheikh, and S. C. Mukhopadhyay, *High Sensitivity Magnetometers*, vol. 19, 1st ed. Cham, Switzerland: Springer, 2017.

[17] S. A. C. Harmon, M. J. Hall, S. Turner, and N. Hillier, "Characterization of magnetic sensors at the operational temperatures of industrial applications," *IEEE Trans. Magn.*, vol. 51, no. 1, Jan. 2015, Art. no. 4001504.

[18] L. Yu *et al.*, "Error compensation and implementation of embedded high-precision magnetometer," in *Proc. Int. Conf. Elect. Control Eng.*, Jun. 2010, pp. 911–914.

[19] C. Petridis, A. Ktena, E. Laskaris, P. Dimitropoulos, and E. Hristoforou, "Ni–Fe thin film coated cu wires for field sensing applications," *Sensor Lett.*, vol. 5, no. 1, pp. 93–97, Mar. 2007.

[20] P. D. Dimitropoulos, J. N. Avaritsiotis, and E. Hristoforou, "Boosting the performance of miniature fluxgates with novel signal extraction techniques," *Sens. Actuators A, Phys.*, vol. 90, nos. 1–2, pp. 56–72, May 2001.

[21] *1 and 2 Axis Magnetic Sensors HMC1001/1002/1021/1022*, Honeywell, Charlotte, NC, USA, 2019. [Online]. Available: https://aerospace.honeywell.com/en/learn/products/sensors/low-field-high-precision-linear-1-and-2-axis-analog-magnetic-sen

[22] I. Georgakopoulos, N. Hadjigeorgiou, and P. P. Sotiriadis, "A CMOS closed loop AMR sensor architecture," in *Proc. Panhellenic Conf. Electron. Telecommun. (PACET)*, Nov. 2017, pp. 1–4.

[23] P. D. Dimitropoulos, J. N. Avaritsiotis, and E. Hristoforou, "A novel micro-Fluxgate sensor based on the AMR effect of ferromagnetic film-resistors," *Sens. Actuators A, Phys.*, vol. 107, no. 3, pp. 238–247, Nov. 2003.

[24] A. Bartók, L. Daniel, and A. Razek, "A multiscale model for thin film AMR sensors," *J. Magn. Magn. Mater.*, vol. 326, pp. 116–122, Jan. 2013.

[25] P. Ripka, M. Tondra, J. Stokes, and R. Beech, "AC-driven AMR and GMR magnetoresistors," *Sens. Actuators A, Phys.*, vol. 76, nos. 1–3, pp. 225–230, Aug. 1999.

[26] P. Ripka, M. Janosek, and M. Butta, "Crossfield sensitivity in AMR sensors," *IEEE Trans. Magn.*, vol. 45, no. 10, pp. 4514–4517, Oct. 2009.

[27] P. Ripka, M. Janosek, M. Butta, S. W. Billingsley, and E. Wakefield, "Crossfield effect in magnetic sensors," in *Proc. IEEE Sensors*, Oct. 2009, pp. 1860–1863.

[28] V. Petrucha, V. Fura, and A. Platil, "Cross-field effect in a triaxial AMR magnetometer with vector and individual compensation of a measured magnetic field," *IEEE Trans. Magn.*, vol. 53, no. 4, Apr. 2017, Art. no. 4000305.

[29] J. Ouyang *et al.*, "Compensation method of cross-axis effect for AMR sensor," in *Proc. Int. Conf. Elect. Control Eng.*, Jun. 2010, pp. 603–606.

[30] N. Hadjigeorgiou, E. Hristoforou, and P. P. Sotiriadis, "Closed-loop current-feedback, signal-chopped, low noise AMR sensor with high linearity," in *Proc. 6th Int. Conf. Mod. Circuits Syst. Technol. (MOCAST)*, May 2017, pp. 1–4.

[31] NASA's Langley Research Center. (Aug. 18, 2019). *Wide Bandwidth Magnetoresistive Eddy Current Probe*. [Online]. Available: https://technology.nasa.gov/patent/LAR-TOPS-96

[32] R. A. Wincheski and J. W. Simpson, "Eddy current probe for surface and sub-surface inspection," U.S. Patent 20120274319 A1, Nov. 1, 2012.

Neoclis G. Hadjigeorgiou (S'16) received the Diploma degree in electrical and computer engineering and the M.S. degree in mechanical engineering from the National Technical University of Athens, Greece, in 2011 and 2013, respectively, where he is currently pursuing the Ph.D. degree in the subject "Integrated Architectures for Magnetic Sensors" in electrical and computer engineering.

From 2013 to 2014, he was a Research Assistant with the Laboratory of Metallurgy in Mining & Metallurgical Engineering, National Technical University of Athens, Greece. He has authored or coauthored some technical articles in the IEEE conferences and some non-IEEE journals. He published a book chapter in the book *Electromagnetic Compatibility for Space Systems Design* (IGI-Global, 2018). His research interests include circuit design, magnetic sensor design, parallel programming, and GPU programming.

Paul P. Sotiriadis (SM'09) received the Diploma degree in electrical and computer engineering from the Electrical and Computer Engineering Department, National Technical University of Athens, Greece, the M.S. degree in electrical engineering from Stanford University, CA, USA, and the Ph.D. degree in electrical engineering and computer science from the Massachusetts Institute of Technology, Cambridge, MA, USA, in 2002.

In 2002, he joined as an Assistant Professor of Electrical and Computer Engineering with Johns Hopkins University. In 2012, he joined the Faculty of the Electrical and Computer Engineering Department, National Technical University of Athens. He is a Faculty Member with the Electrical and Computer Engineering Department, National Technical University of Athens, Greece, where he is also the Director of the Electronics Laboratory. He has authored or coauthored more than 130 technical articles in IEEE journals and conferences and has contributed chapters to technical books. He holds one patent and has several pending patents. His research interests include design, optimization, and mathematical modeling of analog and mixed-signal circuits, RF and microwave circuits, advanced frequency synthesis, biomedical instrumentation, and interconnect networks in deep-submicrometer technologies. He has led several projects in these fields funded by U.S. organizations and has collaborations with industry and national labs.

Dr. Sotiriadis has received several awards, including the 2012 Guillemin-Cauer Award from the IEEE Circuits and Systems Society, the Best Paper Award from the IEEE International Symposium on Circuits and Systems in 2007, the Best Paper Award from the IEEE International Frequency Control Symposium in 2012, and the Best Paper Award from the IEEE International Conference on Modern Circuits and Systems Technologies in 2019. He regularly reviews for many IEEE Transactions and conferences and serves on proposal review panels. He is an Associate Editor of the IEEE TRANSACTIONS ON CIRCUITS AND SYSTEMS – I and the IEEE SENSORS JOURNAL, has served as an Associate Editor for the IEEE TRANSACTIONS ON CIRCUITS AND SYSTEMS – II from 2005 to 2010, and has been a member of technical committees of many conferences.